crystals

MDPI

Article

Anomalous Ferromagnetic Phase in the $Gd_{1-x}Er_xB_4$ Series: Crystal Growth, Thermal, and Magnetic Properties

Sueli H. Masunaga [1,2,*], Vagner B. Barbeta [1], Fábio Abud [2,3], Milton S. Torikachvili [4] and Renato F. Jardim [2]

[1] Departamento de Física, Centro Universitário FEI, São Bernardo do Campo 09850-901, SP, Brazil; vbarbeta@fei.edu.br
[2] Instituto de Física, Universidade de São Paulo, São Paulo 05315-970, SP, Brazil; fabio.abud@usp.br (F.A.); rjardim@if.usp.br (R.F.J.)
[3] Escola de Engenharia de Lorena, Departamento de Engenharia de Materiais, Universidade de São Paulo, Lorena 12612-550, SP, Brazil
[4] Department of Physics, San Diego State University, San Diego, CA 92182, USA; miltont@sdsu.edu
* Correspondence: sueli.masunaga@gmail.com

Abstract: Rare-earth tetraborides RB_4 are of great interest due to the occurrence of geometric magnetic frustration and corresponding unusual magnetic properties. While the Gd^{3+} spins in GdB_4 align along the *ab* plane, Er^{3+} spins in the isomorphic ErB_4 are confined to the *c*–axis. The magnetization in the latter exhibits a plateau at the midpoint of the saturation magnetization. Therefore, solid solutions of (Gd, Er)B_4 provide an excellent playground for exploring the intricate magnetic behavior in these compounds. Single crystals of $Gd_{1-x}Er_xB_4$ (x = 0, 0.2, and 0.4) were grown in aluminum flux. X-ray diffraction scans revealed single-phase materials, and a drop in the unit cell volume with increasing Er content, suggesting the partial substitution of Er at the Gd sites. Heat capacity measurements indicated a systematic decrease of the Néel temperature (T_N) with increasing Er content. The effective magnetic moment determined from the magnetization measurement agreed with the calculated free ion values for Gd^{3+} and Er^{3+}, providing further evidence for the successful substitution of Er for Gd. The partial substitution resulted in an anomalous ferromagnetic phase below T_N, exhibiting significant anisotropy, predominantly along the *c*-axis. This intriguing behavior merits further studies of the magnetism in the $Gd_{1-x}Er_xB_4$ borides.

Keywords: tetraborides; susceptibility; specific heat; geometric magnetic frustration; antiferromagnetism; flux method; Shastry–Sutherland; induced ferromagnetism

Citation: Masunaga, S.H.; Barbeta, V.B.; Abud, F.; Torikachvili, M.S.; Jardim, R.F. Anomalous Ferromagnetic Phase in the $Gd_{1-x}Er_xB_4$ Series: Crystal Growth, Thermal, and Magnetic Properties. *Crystals* **2023**, *13*, 1137. https://doi.org/10.3390/cryst13071137

Academic Editor: Sergey L. Bud'ko

Received: 5 July 2023
Revised: 17 July 2023
Accepted: 18 July 2023
Published: 21 July 2023

1. Introduction

Motivated by their interesting magnetic properties, the rare-earth tetraborides with general formula RB_4 (R = rare earth) have been studied for many years [1–3]. These compounds are metallic conductors and show antiferromagnetic (AF) ordering, except for R = Pr, which is ferromagnetic (FM) [2]. The indirect coupling between the magnetic ions is of the Ruderman–Kittel–Kasuya–Yosida type (RKKY) [2]. The crystal structure is tetragonal belonging to the symmetry group $P4/mbm$. Due to the nature of the crystal structure, these compounds exhibit strongly anisotropic magnetic and electrical properties [4,5].

The magnetic sublattice of R ions in RB_4 consists of 2d orthogonal R–R dimers in the *ab*-plane, forming squares and triangles [6]. The bond length between the rare earth nearest-neighbor dimmer (NN) is very close to the next-nearest neighbor (NNN). Therefore, one can presume that the corresponding magnetic interactions J_1 and J_2, as shown in Figure 1, are also close to each other. If the magnetic interaction between the rare-earth ions is antiferromagnetic, it is likely that the system should exhibit geometrically frustrated magnetic interactions, consistently with the theoretical approach described in the Shastry–Sutherland lattice (SSL) [6–8].

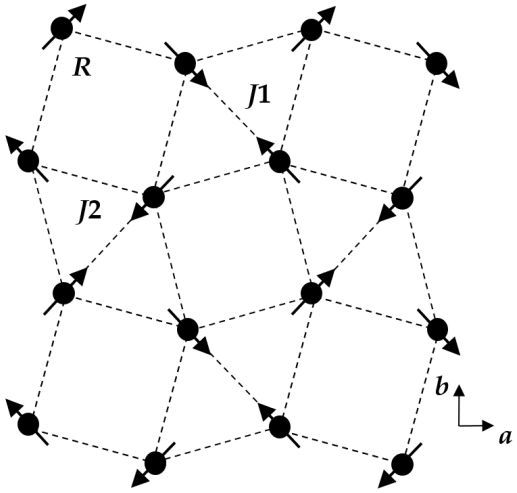

Figure 1. Exchange interactions J_1 and J_2 between NN and NNN rare-earth (R) ions in RB_4. The arrows indicate the spin projection in the *ab*-plane of the non-collinear magnetic structure of GdB_4.

There are some noteworthy differences between GdB_4 and ErB_4. All heavy RB_4 (R = Tb, Dy, Ho, Er, Tm) display strong Ising-like anisotropies, resulting in the rare-earth magnetic moments being oriented preferably along the *c*-axis or along the *ab*-plane. The Er^{3+} ions in ErB_4 have a large total angular moment $J = 15/2$. It shows an antiferromagnetic transition at T_N = 15.4 K, with an easy axis orientation along the *c* direction [9], and the magnetic moment was previously determined to be 8.2 $\pm$ 0.6 μ_B [10]. The $M \times H$ curve exhibits a plateau region at the midpoint of the saturation magnetization (M_S) value. In this plateau phase, half of the Er^{3+} magnetic moments flip in the field direction, and it is suggestive of the formation of ferromagnetic and antiferromagnetic stripe structures, like domain [11]. The attempt to theoretically describe the system in terms of an effective spin-1/2 Shastry–Sutherland model under strong Ising anisotropy could show the $M_S/3$ plateau, but it was not able to reproduce the appearance of the $M_S/2$ phase. The inclusion of interactions of longer ranges seems to be a necessary ingredient to reproduce the experimentally observed results [12].

In contrast, the Gd^{3+} magnetic moments in GdB_4 align perpendicularly to the *c*-axis, i.e., along the basal *ab*-plane [13]. No plateau is observed in $M \times H$ curves, and the antiferromagnetic ordering temperature for GdB_4 is T_N = 42 K [2,14]. Spherical neutron polarimetry revealed that the magnetic spins order non-collinearly (see Figure 1), in a structure with the Shubnikov magnetic space group $P4/m'b'm'$. The magnetic moment of Gd^{3+} was determined to be 7.14 $\pm$ 0.17 μ_B, quite close to the free ion value [13].

Many recent papers have focused on the potential applications of rare earth borides. For example, the strong geometrical frustration and competing exchange interactions in these materials indicate their promising application as materials with enhanced magnetocaloric effect [15]. Composite ceramics of RB_6 and RB_4 have been proposed to be used as a new type of high-performance electromagnetic wave-absorbing material that could help to diminish interference and electromagnetic pollution [16]. Also, their good thermal conductivity, resistance to oxidation, and hardness make them suitable for use as coatings for cutting tools, turbine blades, and other high-wear components, as well as for high-temperature applications [17].

The perturbation of the intricate balance between competing exchange interactions within a geometrically frustrated magnetic system can generate novel electronic and magnetic states, resulting from the interaction between frustrated spins and lattice, orbital, and charge degrees of freedom [18]. Hence, considering the rich phase diagram exhibited by rare-earth borides, investigations into these materials, as well as the effects produced by different kinds of doping, remain subjects of significant interest [19]. Therefore, the goal of this work is to probe the thermal and magnetic properties of $Gd_{1-x}Er_xB_4$ (x = 0–0.4).

Single crystals were grown from aluminum flux, and analyzed by means of Laue X-ray images, and powder X-ray diffraction (XRD). Measurements of magnetization [$M(T, H)$] and heat capacity [$C_p(T, H)$] were carried out with magnetic fields applied parallel and perpendicular to the *c*-axis. These measurements permitted monitoring the fast evolution of the magnetic properties upon the partial substitution of Er for Gd in GdB_4. We have observed an anomalous and highly anisotropic ferromagnetic phase within the geometrically frustrated magnetic system of $Gd_{1-x}Er_xB_4$.

2. Materials and Methods

Stoichiometric amounts of high purity Gd (Merch 99.9%), Er (Merch 99.9%), and B (Alfa Aesar 99.99%) corresponding to the $Gd_{1-x}Er_xB_4$ (x = 0.2, and 0.4) compositions and high-purity aluminum shots (Alfa Aesar 99.99%) were placed in 70 mL alumina crucibles, in 5–95% amounts by weight, respectively. The alumina crucibles were loaded on a vertical tube furnace under flowing ultra-high pure argon gas, heated and maintained at 1500 °C for one hour, cooled slowly to 1000 °C, and fast-cooled to ambient temperature by turning the furnace off. The $Gd_{1-x}Er_xB_4$ crystals were separated from the flux by dissolving the aluminum in a saturated NaOH solution. Laue photographs were taken by back-reflection methodology to assess the quality of the single crystals and determine the crystallographic orientation [20]. The open source software QLaue (Beta) was used to simulate the diffraction spots [21]. GdB_4 single crystals were previously grown and characterized using the same methodology, as detailed elsewhere [22].

Ambient temperature X-ray powder diffraction was carried out on a few crystals crushed in an agate mortar, using the CuK_α radiation of a D-8 Discovery diffractometer in the $15 \leq 2\theta \leq 120^\circ$ range. The characterization of the GdB_4 single crystal is described elsewhere [22]. The grown GdB_4 crystals had plate-like polyhedral morphology; the largest dimension could reach $\approx$ 1.5 mm, and the larger facets corresponded to the (110) and (001) planes.

Specific heat $C_p(T, H)$ and magnetization $M(T, H)$ measurements of the $Gd_{1-x}Er_xB_4$ crystals were obtained with a physical property measurement system (PPMS) from Quantum Design. The $C_p(T, H)$ data of x = 0, 0.2, and 0.4 compositions were collected in the 2–100 K temperature range in applied magnetic fields up to 9 T applied both parallel and perpendicular to the *c*-direction. The $M(T, H)$ data of x = 0.2 and 0.4 samples were collected in the 2–300 K temperature range in applied magnetic fields up to 9 T applied both parallel and perpendicular to the *c*-direction. The magnetic properties of GdB_4 have been previously investigated and reported in Ref. [22].

3. Results and Discussion

3.1. Samples and X-ray Diffraction

The flux growth method for the synthesis of $Gd_{1-x}Er_xB_4$ (x = 0.2 and 0.4) crystals yielded platelets with typical dimensions of $\approx$ 1.5 mm $\times$ 1.5 mm $\times$ 0.5 mm, as shown in Figure 2. The X-ray Laue images displayed in Figures 3 and 4 indicate that the larger facets are perpendicular to the crystallographic *c*-direction. The orientation of the crystals was determined from the Laue images using the QLaue software. The lack of distortion or smearing in the diffraction spots of Figures 3 and 4 is suggestive of high crystallinity, with the absence of defects or twining. The crystal morphology was suitable for assembling and measuring the physical properties parallel and perpendicular to the *c*-axis, as discussed in the following sections.

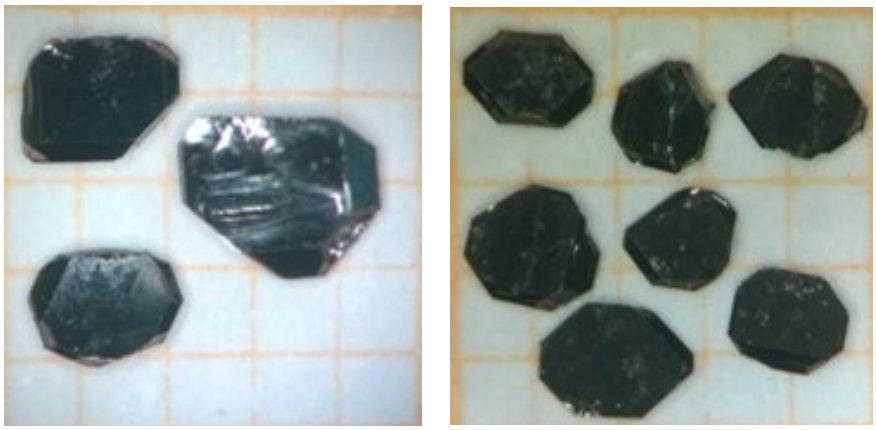

(**a**) (**b**)

Figure 2. Images of (**a**) $Gd_{0.8}Er_{0.2}B_4$ and (**b**) $Gd_{0.6}Er_{0.4}B_4$ single crystals grown by the flux method, placed on a 1 mm grid paper.

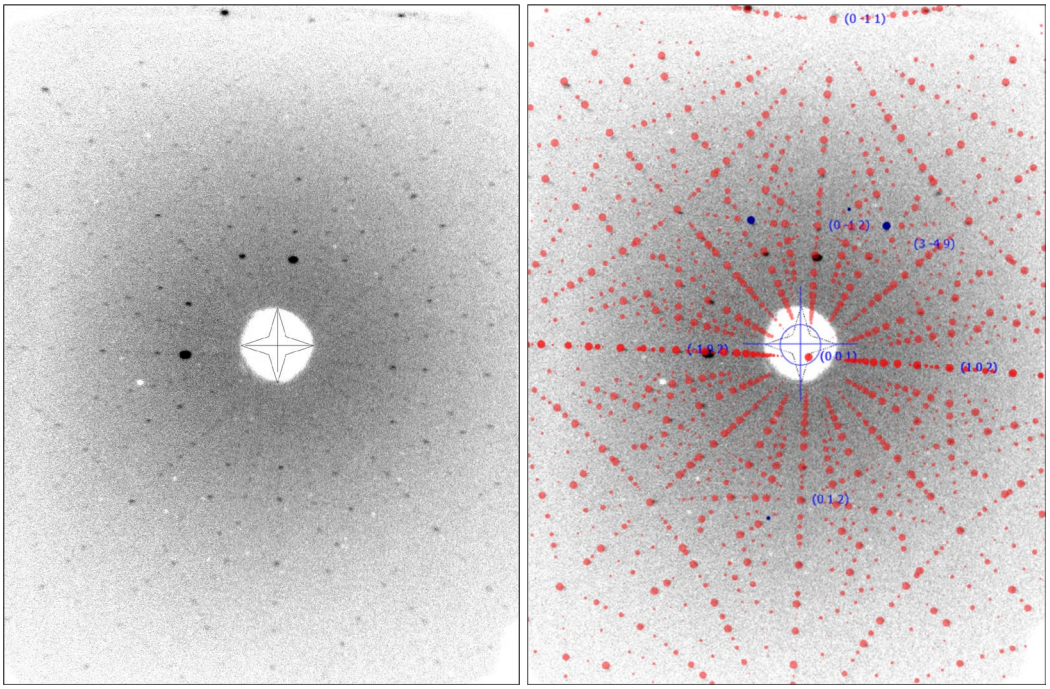

Figure 3. Laue X-ray diffraction photograph and the simulated pattern showing the (001) plane for $Gd_{0.8}Er_{0.2}B_4$.

Structural refinement of the $Gd_{1-x}Er_xB_4$ (x = 0.2, and 0.4) crystals were carried out using the General Structure Analysis System - II (GSAS-II) software based on the Rietveld methodology [23], and the results are shown in Figure 5. The XRD patterns do not show the presence of additional phases, and the lattice parameters resulting from the refinement are listed in Table 1, alongside our previously reported data for GdB_4 [22] and data from the literature for ErB_4 [10]. These compounds crystallize in a tetragonal structure at room temperature, $P4/mbm$ (No. 127). The (001) Bragg reflection shifts towards higher 2θ values upon the partial substitution of Er for Gd, as shown in the inset of Figure 5b, a result consistent with the smaller ionic radius of Er [24], and, in turn, a drop of the unit cell volume.

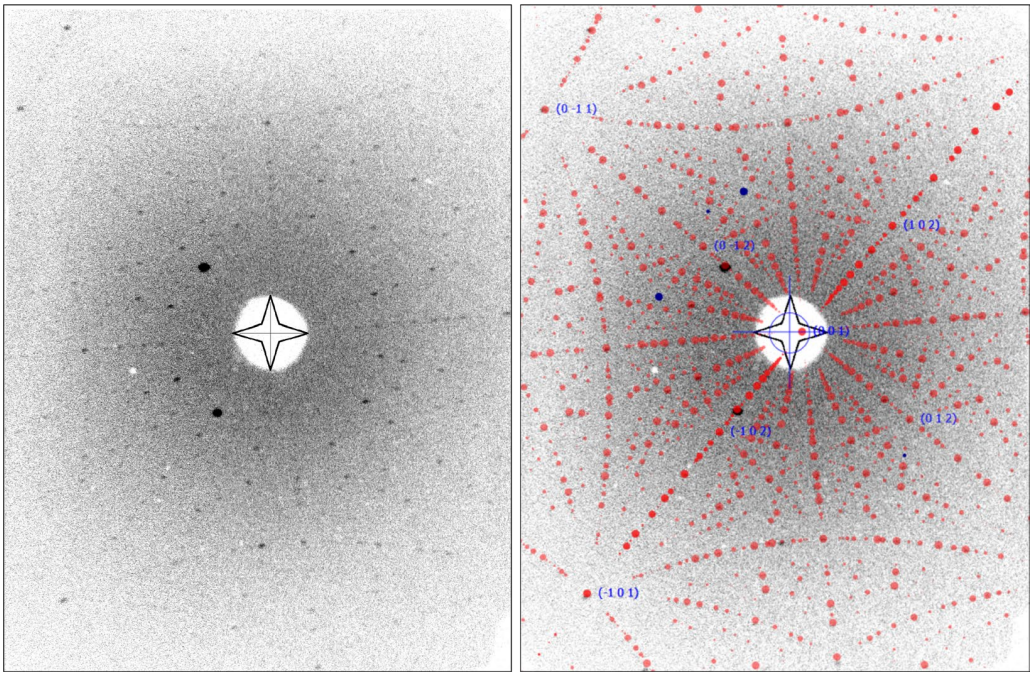

Figure 4. Laue X-ray diffraction photograph and the simulated pattern showing the (001) plane for $Gd_{0.6}Er_{0.4}B_4$.

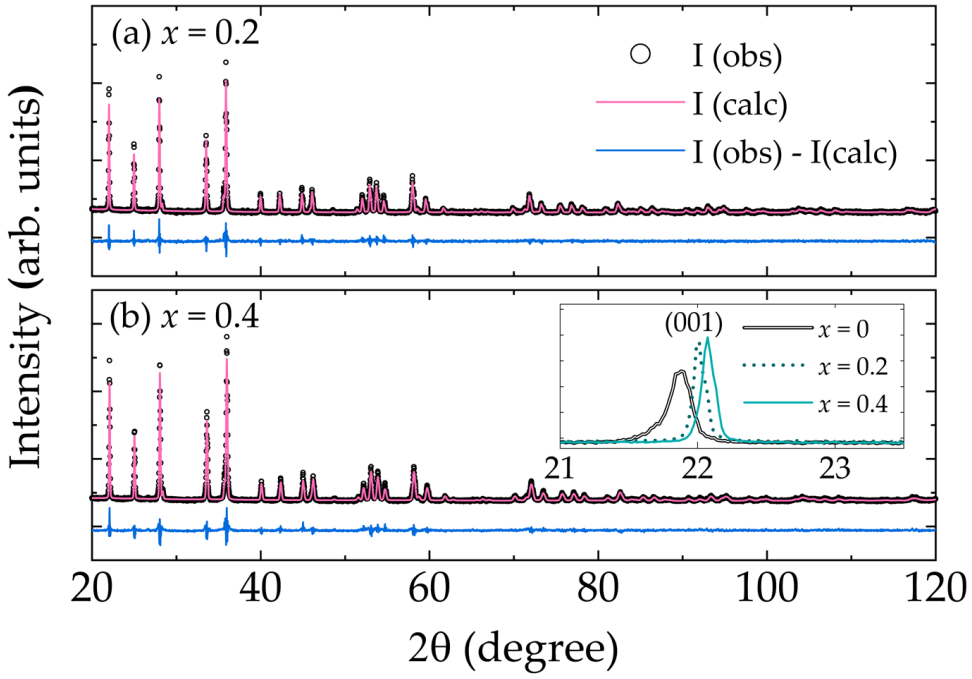

Figure 5. Ambient temperature XRD patterns (symbols) for (**a**) $Gd_{0.8}Er_{0.2}B_4$, and (**b**) $Gd_{0.6}Er_{0.4}B_4$. Corresponding calculated patterns are shown in solid red lines and the difference between experimental and calculated intensities in solid blue lines. The inset displays an expanded view of the (001) reflection for $Gd_{1-x}Er_xB_4$ (x = 0, 0.2, and 0.4).

Table 1. Crystal structure data and refinement for $Gd_{1-x}Er_xB_4$ (x = 0, 0.2, 0.4, and 1.0).

x	a, b (Å)	c (Å)	χ^2
0 [1]	7.1421 (2)	4.0467 (2)	1.7
0.2	7.1298 (2)	4.0377 (2)	2.9
0.4	7.1133 (7)	4.0264 (5)	4.1
1.0 [2]	7.071 (3)	4.000 (1)	–

[1] Data from Ref. [22]. [2] Data from Ref. [10].

Given the different magnetic structures of GdB_4 and ErB_4, the progressive substitution of Er for Gd in the $Gd_{1-x}Er_xB_4$ is quite likely to affect the magnetic and thermal properties. We monitored these changes by measuring $M(T, H)$ and $C_p(T)$ respectively.

3.2. Specific Heat

The zero-field specific heat $C_p(T)$ measurements were conducted on all three samples of $Gd_{1-x}Er_xB_4$ (x = 0, 0.2, and 0.4) for the present investigation, and the obtained $C_p(T)$ data are shown in Figure 6a. The $C_p(T)$ curve for the undoped GdB_4 clearly shows a pronounced peak at the Néel temperature T_N = 41.8 K, indicating a transition from a paramagnetic (PM) to an antiferromagnetic (AFM) phase. Upon the partial substitution of Er for Gd, the magnetic ordering feature shifts to lower temperatures, reaching 31.8 and 26.8 K for $Gd_{0.8}Er_{0.2}B_4$ and $Gd_{0.6}Er_{0.4}B_4$, respectively. A small bump centered near $T \approx 10$ K is observed in GdB_4, a feature frequently observed in other lanthanide compounds and attributed to the Schottky contribution to the heat capacity [25]. The occurrence of this feature remains in the x = 0.2 sample but is much more suppressed in the x = 0.4 crystal. Previous studies have shown that the Schottky contribution to the heat capacity in ErB_4 occurs at higher temperatures [26].

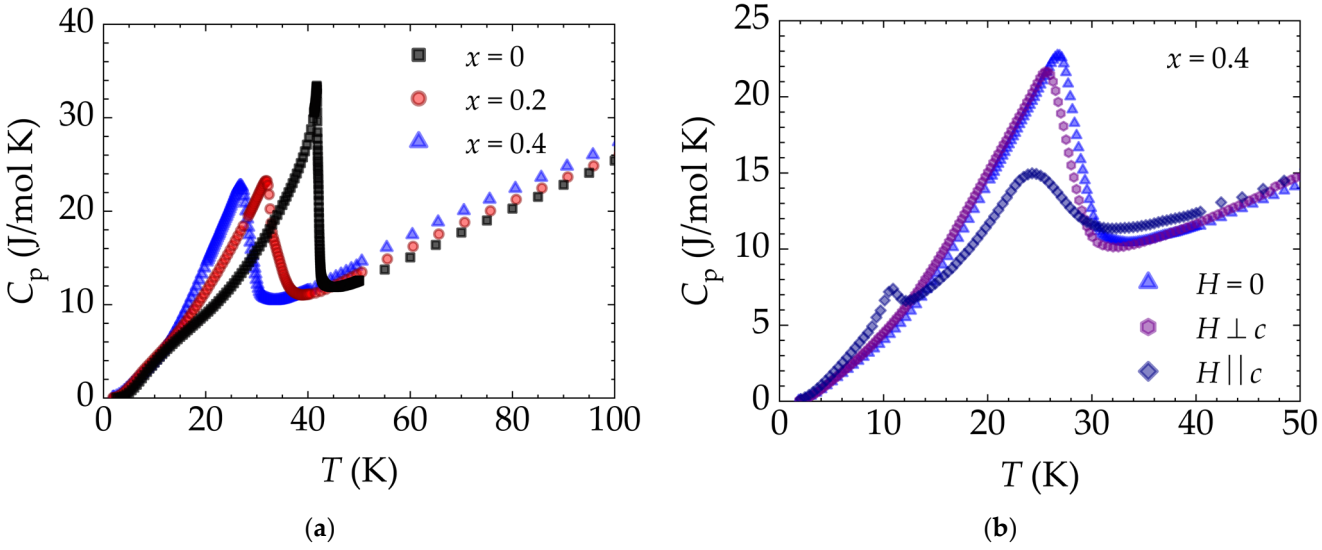

Figure 6. (**a**) Zero-field temperature dependence of the specific heat $C_p(T)$ for $Gd_{1-x}Er_xB_4$ (x = 0, 0.2, and 0.4); (**b**) $C_p(T)$ for x = 0.4 measured in H = 0 and H = 5 T, with field applied parallel and perpendicular to the c-axis.

At low temperatures, the heat capacity can be approximated by the relation $C_p = C_{el} + C_{latt} + C_{sch} + C_m$, where C_{el}, C_{latt}, C_{sch}, and C_m are the contributions due to the electron system, phonon, Schottky anomaly, and magnetic subsystem, respectively. To probe the effect of the partial change of Er for Gd in the sample magnetism, the magnetic contribution C_m for each composition was estimated, as depicted in Figure 7b. The phonon contribution C_{latt} was estimated using the method described by Stout and Catalano [27], which relies on measuring the heat capacity C_p of a nonmagnetic isomorph, which in this case was YB_4.

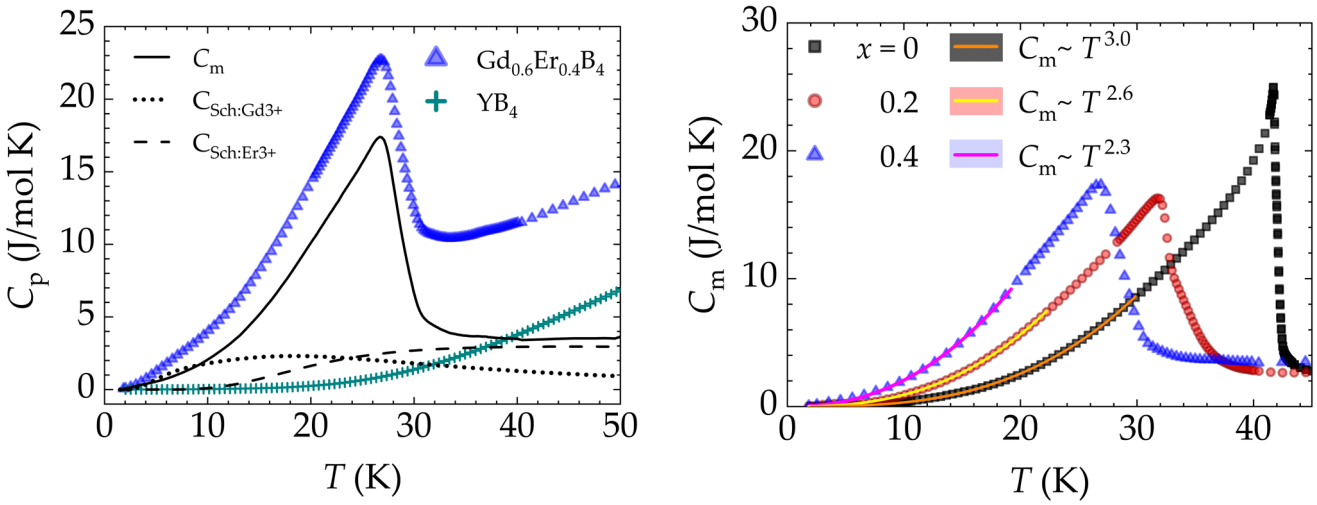

Figure 7. (**a**) Specific heat for $Gd_{0.6}Er_{0.4}B_4$, YB_4, and estimated values of C_m and C_{sch}.; (**b**) $C_p(T)$ magnetic heat capacity for $Gd_{1-x}Er_xB_4$ (x = 0, 0.2, and 0.4). Solid lines are fits to AT^{α}.

The heat capacity of YB_4 at low temperatures can be expressed as $C_{p:YB4} = C_{el} + C_{latt} = aT + bT^3$, where $a = 12 \times 10^{-4}$ J/mol K^2 and $b = 2.1 \times 10^{-5}$ J/mol K^4, values obtained by fitting. Comparable values of a and b have been reported for GdB_4 ($a = 5.96 \times 10^{-4}$ J/mol K^2 and $b = 4.89 \times 10^{-5}$ J/mol K^4) and ErB_4 ($a = 8.46 \times 10^{-4}$ J/mol K^2 and $b = 6.82 \times 10^{-5}$ J/mol K^4) in previous studies [25,26]. Therefore, it is reasonable to assume that the contributions of C_{el} and C_{latt} to the heat capacity of the $Gd_{1-x}Er_xB_4$ series are like those of YB_4. Consequently, the specific heat of YB_4 was subtracted from the specific heat of the $Gd_{1-x}Er_xB_4$ series, enabling the determination of the specific heat associated with the Schottky and magnetic anomalies.

The contribution to the specific heat due to the Schottky anomaly C_{sch} for a system with n levels, separated by energies ε_n and with degeneracy g_n, is given by

$$C_{sch} = R\frac{g_1\left(\frac{\varepsilon_1}{T}\right)^2 e^{-\frac{\varepsilon_1}{T}} + g_2\left(\frac{\varepsilon_2}{T}\right)^2 e^{-\frac{\varepsilon_2}{T}} + \cdots}{g_0 + g_1 e^{-\frac{\varepsilon_1}{T}} + g_2 e^{-\frac{\varepsilon_2}{T}} + \cdots} - R\left(\frac{g_1\left(\frac{\varepsilon_1}{T}\right) e^{-\frac{\varepsilon_1}{T}} + g_2\left(\frac{\varepsilon_2}{T}\right) e^{-\frac{\varepsilon_2}{T}} + \cdots}{g_0 + g_1 e^{-\frac{\varepsilon_1}{T}} + g_2 e^{-\frac{\varepsilon_2}{T}} + \cdots}\right)^2, \quad (1)$$

where R is the ideal gas constant and ε_n is given in units of kelvin [28]. The C_{sch} curve for all samples was obtained by fitting the data below T_N using the equation $C = AT^{\alpha} + C_{sch}$, where AT^{α} represents the magnetic specific heat contribution, with $\alpha = 3$ for AFM systems. As initial parameters for the Schottky anomaly, the data from Ref. [25] for Gd^{3+} were used, where $g_0 = 2$, $g_1 = 2$, $g_2 = 4$, $\varepsilon_1 = 30$ K, and $\varepsilon_2 = 75$ K. For Er^{3+}, the data from Ref. [26] are $g_0 = 2$, $g_1 = 4$, $g_2 = 6$, $g_3 = 4$, $\varepsilon_1 = 85$ K, $\varepsilon_2 = 240$ K, and $\varepsilon_3 = 700$ K. For the fitting procedure, only ε_1 and ε_2 for Gd^{3+} were free parameters. The parameters for Er^{3+} were kept fixed since initial fits indicated their values did not vary significantly. Thus, C_m was obtained by subtracting the fitted C_{sch}, considering the proportional contribution due to the Gd^{3+} and Er^{3+}.

The different contributions to the total specific heat are shown in Figure 7a, for the $x = 0.4$ sample. After isolating the C_m curve, its temperature dependence was investigated by fitting to the equation AT^{α} for temperatures up to $0.7T_N$, as shown in Figure 7b. For GdB_4, $\alpha = 3$, as expected for antiferromagnetic systems. The exponent α decreases to 2.6 and 2.3 for the samples with $x = 0.2$ and 0.4, respectively, approaching the 1.5 value, expected for ferromagnetic systems. This is an indication of a change in the system's ordering, due to the possible competition between magnetic anisotropies.

In order to probe the competition between magnetic anisotropies, we have performed measurements of $C_p(T, H)$ in magnetic fields H up to 9 T. Shown in Figure 6b is the effect of a magnetic field $H = 5$ T applied along the two different crystallographic directions in

$Gd_{0.6}Er_{0.4}B_4$, resulting in a drop in the temperature of the C_p peak at T_N, and a significant change in morphology for $H//c$. In general, for fields in the $0 \leq H \leq +9$ T range, the value of T_N drops by ~15% and ~7% for fields applied parallel and perpendicular to the *c*-axis, respectively. In contrast, $C_p(T)$ for the $Gd_{0.8}Er_{0.2}B_4$ is nearly insensitive to the magnetic field, with the value of T_N dropping but staying within 3% of the zero-field value, for both orientations.

In addition to the main feature at T_N, the $C_p(T)$ data for $Gd_{0.6}Er_{0.4}B_4$, shown in Figure 6b, presents a second feature at low temperatures, centered near 10 K, when a 5 T magnetic field is applied parallel to the *c*-axis. This peak, observed only in $Gd_{0.6}Er_{0.4}B_4$, is possibly due to a metamagnetic transition, occurring exclusively along the *c*-axis, as suggested by the magnetization data.

3.3. Magnetization

The temperature-dependent magnetic susceptibility curves $\chi = (M/H) \times T$ for $Gd_{1-x}Er_xB_4$ (x = 0.2 and 0.4), taken in 0.5 T magnetic fields parallel or perpendicular to the *c*-axis, are shown in Figure 8. The maximum value of χ occurs approximately at the same T_N determined from the $C_p(T)$ measurements of Figure 6. The value of T_N was taken from the minimum of the second derivatives $d^2\chi/dT^2$. Consistently with the $C_p(T)$ data, T_N drops with the Er concentration, as shown in the inset of Figure 8b.

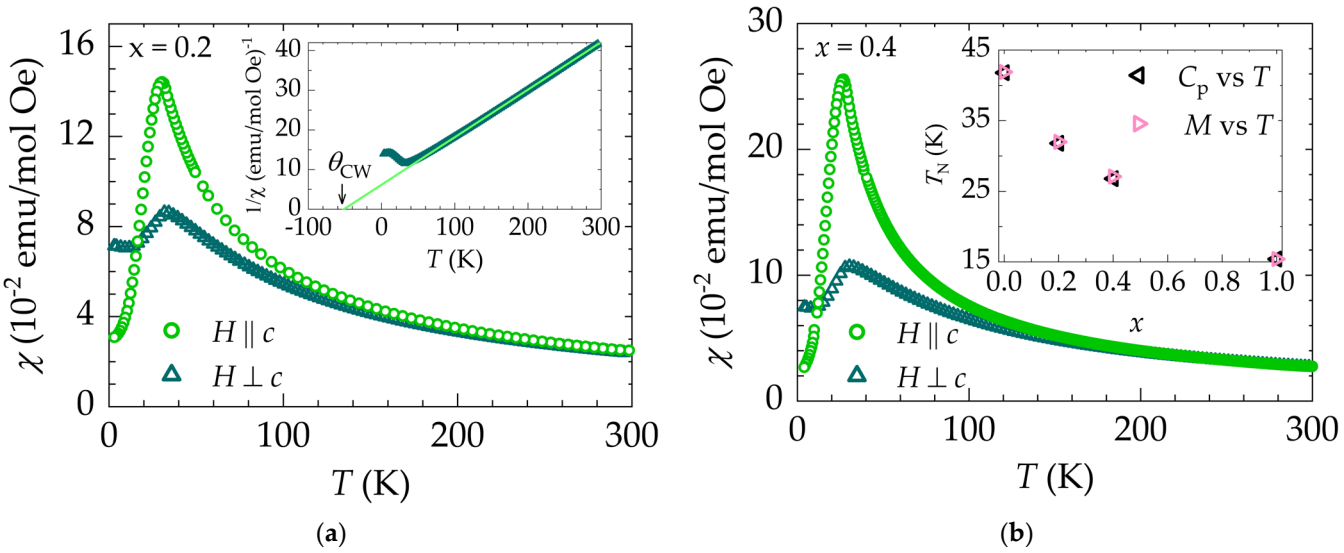

Figure 8. Temperature dependence of the magnetic susceptibility for (**a**) $Gd_{0.8}Er_{0.2}B_4$ and (**b**) $Gd_{0.6}Er_{0.4}B_4$. The applied magnetic field parallel or perpendicular to the *c*-axis was 0.5 T. The inset in (**a**) shows $1/\chi(T)$ for a field perpendicular to the *c*-axis and the corresponding value of θ_{CW}. The inset in (**b**) displays the Néel temperature for different Er concentrations at zero applied fields (T_N for x = 1.0 was obtained from Ref. [9]).

For both x = 0.2 and x = 0.4 samples, χ (T) exhibits anisotropic behavior up to ~150 K, a temperature considerably higher than T_N. In contrast, the undoped GdB_4 displays anisotropic χ (T) behavior only below T_N. Notably, the partial substitution of 20% Er seems to be sufficient to induce this anisotropic behavior, reminiscent of the behavior in ErB_4 [9]. To gauge the magnitude of the anisotropy at 4 K, we calculated the ratio of the susceptibilities perpendicular and parallel to the *c*-axis and obtained 2.3 and 2.8 for x = 0.2 and 0.4, respectively. On the other hand, the susceptibilities parallel to the *c*-axis are higher near T_N, exhibiting a magnitude of 1.7 and 2.8 times greater than the perpendicular susceptibility for the x = 0.2 and x = 0.4 samples, respectively. The magnetic susceptibility data for $Gd_{0.8}Er_{0.2}B_4$ show that the substitution of 20% of Er favors the *c*-axis for spins alignment since χ tends to lower values with decreasing temperature, while the perpendicular susceptibility shows a small temperature dependence.

As shown in the inset of Figure 8a for $Gd_{0.8}Er_{0.2}B_4$, the magnetic susceptibility (χ) in the PM region follows the Curie–Weiss law [29]

$$\chi = \frac{C}{T - \theta_{CW}}, \tag{2}$$

where θ_{CW} is the Curie–Weiss constant, which is usually associated with the magnetic interactions between PM ions, expressed in units of temperature, and C is the Curie constant, given by

$$C = \frac{N_a \mu_{eff}^2}{3k_B}. \tag{3}$$

Here, N_a is the Avogadro's number, k_B the Boltzmann constant, and μ_{eff} the effective magnetic moment, calculated from

$$\mu_{eff} = g_J[J(J+1)]^{1/2}\mu_B, \tag{4}$$

where g_J is the Landé g-factor, J the total quantum number, and μ_B the Bohr magneton. The theoretical values of μ_{eff} calculated for Gd^{3+} and Er^{3+} are 7.94 and 9.58 μ_B, respectively.

For the $Gd_{1-x}Er_xB_4$ solid solutions, the theoretical values of μ_{eff} can be approximately obtained from

$$\mu_{eff} = \left[(1-x)\mu_{eff_{Gd}}^2 + x\mu_{eff_{Er}}^2\right]^{1/2}. \tag{5}$$

On the other hand, the experimental values of μ_{eff} can be obtained by fitting the $(1/\chi)$ vs. T data to the expression

$$\frac{1}{\chi} = \frac{8(T - \theta_{CW})}{\mu_{eff}^2}, \tag{6}$$

resulting from combining Equations (2) and (3), with $N_a = 6.022 \cdot 10^{23}$ mol^{-1}, $k_B = 1.381 \cdot 10^{-16}$ erg/K, and $\mu_B = 9.274 \cdot 10^{-21}$ emu, as shown in the inset of Figure 8a. The experimental values of μ_{eff} obtained from fits of the experimental data to Equation (6) at temperatures above 100 K, are displayed in Table 2. The μ_{eff} values obtained from the $\chi(T)$ data with field along the two crystallographic directions are consistent with the calculated μ_{eff} values for the Gd^{3+} and Er^{3+} free ions, providing additional evidence for the effective partial substitution of Er for Gd within this series.

Table 2. Calculated and experimental values of effective magnetic moment (μ_{eff}) and Curie–Weiss constant (θ_{CW}) for $Gd_{1-x}Er_xB_4$ (x = 0, 0.2, 0.4, and 1.0). μ_{eff}^{calc} values are calculated using Equation (5) and μ_{eff}^{exp} values are obtained from the fittings of $(1/\chi)$ vs. T data to Equation (6).

x	μ_{eff}^{calc} (μ_B)	μ_{eff}^{exp} (μ_B) ($H \| c$)	θ_{CW} (K) ($H \| c$)	μ_{eff}^{exp} (μ_B) ($H \perp c$)	θ_{CW} (K) ($H \perp c$)
0	7.94	7.98	−70	7.94	−66
0.2	8.29	8.20	−39	8.26	−57
0.4	8.63	8.34	−15	8.72	−48
1.0	9.58	9.27 *	+11.24 *	9.50 *	−23.26 *

* Data from Ref. [30].

The data displayed in Table 2 indicate that the effective magnetic moments μ_{eff}^{exp} for GdB_4 and $Gd_{0.8}Er_{0.2}B_4$ are only slightly different for the two orientations of the magnetic field, suggesting that the magnetic anisotropy in these two compositions is very small. Upon normalization with respect to parameters associated with the c-axis, the difference between these values amounts to 0.5% and 0.7% for x = 0 and x = 0.2, respectively. On the other hand, there is a marked difference of 4.6% between the two values for the x = 0.4 composition, a value close to the increased magnetic anisotropy in the $Gd_{0.6}Er_{0.4}B_4$ crystal.

The magnetic anisotropic behavior of $\chi(T)$ is also noted in the Curie–Weiss constant for the x = 0.2 and 0.4 samples. The difference between θ_{CW} values obtained along directions

parallel and perpendicular to the *c*-axis also increase with x. These differences are 5.7%, 46%, and 220% for crystals with x = 0, 0.2, and 0.4, respectively.

The occurrence of appreciable magnetic anisotropy in the $Gd_{1-x}Er_xB_4$ series is also noticeable in the isothermal magnetization curves for x = 0.2 and 0.4 samples, as shown in Figure 9, provided that the magnitudes of magnetization differ significantly when measured along two distinct crystallographic directions. Also, a careful examination of Figure 9b clearly shows an increase in anisotropy with the Er content.

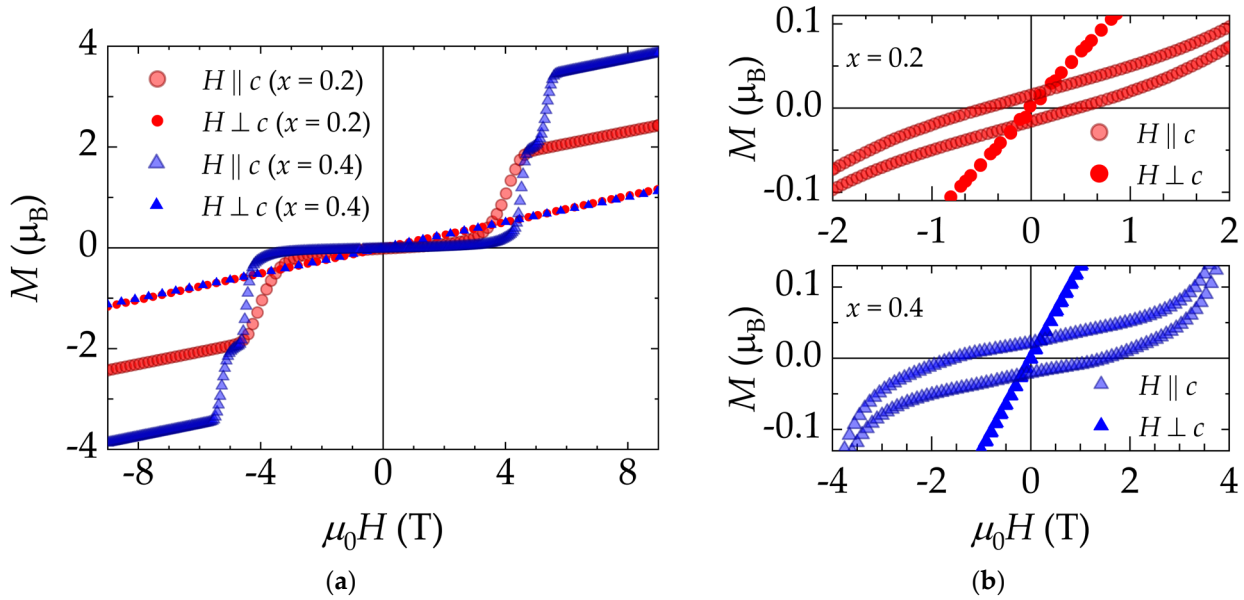

Figure 9. (**a**) Field-dependent magnetization at 5 K for $Gd_{1-x}Er_xB_4$ (x = 0, 0.2, and 0.4) with field parallel (open symbols) and perpendicular (closed symbols) to the *c*-axis; (**b**) expanded view of magnetization curves near H = 0 for x = 0.2 on the upper panel and for x = 0.4 on the lower panel.

Although GdB_4 and ErB_4 are antiferromagnetic systems that exhibit magnetization curves without hysteresis, the x = 0.2 and 0.4 compositions show anomalous remnant magnetization behavior. As shown in Figure 9b, these samples display an appreciable coercive field at 5 K, with H_C values of ~0.46 T and ~1.53 T for x = 0.2 and 0.4, respectively. This anomaly is also significantly anisotropic, i.e., it is more pronounced for H applied along the *c*-axis. In the x = 0.2 sample, a minor hysteresis is observed along the direction perpendicular to the *c*-axis, with an H_C value of ~0.025 T. In addition, for the x = 0.4 sample, the coercive field and remnant magnetization are negligibly small along the (001) plane.

As the applied magnetic field along the *c*-axis increases, $Gd_{0.6}Er_{0.4}B_4$ displays two magnetic transitions for $H \leq 9$ T, as shown in Figure 9a. The first (near 4.5 T) is suggestive of a metamagnetic transition, characterized by a magnetization plateau state occurring at M/M_S = 1/2 , where M_S is the saturation magnetization of the Er^{3+} ions. The second transition corresponds to the full alignment of the Er^{3+} ions along the *c*-axis. The theoretical value of the saturation magnetization per Er^{3+} ion is $M_S = gJ\mu_B = 9\ \mu_B$. Based on this value, the saturation magnetization for the Er^{3+} ions in the x = 0.4 sample corresponds to 3.6 μ_B.

Immediately after a magnetic field of 5.6 T, the transition to the total magnetization of the system reaches a value close to 3.46 μ_B. By subtracting the contribution of the Gd^{3+} ions, the experimental saturation magnetization corresponding to the Er^{3+} ions is 94% of the theoretical value. In this procedure, as a first approximation, we assume that the Gd^{3+} ions contribute linearly to the system's magnetization with H, corresponding to the initial slope of the virgin magnetization curve up to the considered magnetic field of 5.6 T.

Only one field-induced transition is observed for the $Gd_{0.8}Er_{0.2}B_4$ composition, as shown in Figure 9a. Using the same procedure applied for the x = 0.4 composition to

subtract the contribution of the Gd^{3+} ions, the magnetization attributed to the Er^{3+} ions amounts to 99% of the theoretical value of the expected saturation magnetization. These results reveal that the transition to the plateau state only takes place in the $x = 0.4$ sample, while the transition to the field-induced paramagnetic state, corresponding to the full alignment of the magnetic moments of Er^{3+}, occurs for both $x = 0.2$ and $x = 0.4$ compositions.

In contrast, $M \times H$ curves with a field applied perpendicular to the *c*-axis do not show field-induced transitions in fields up to 9 T, as shown in Figure 9. This finding is consistent with the specific heat data of Figure 6b, where a metamagnetic transition is detected as a second peak occurring at low temperatures for a 5 T magnetic field also applied along the *c*-axis. When the same magnitude of a magnetic field is applied perpendicular to the *c*-axis, only a single maximum is observed in the $C_p \times T$ curve, corresponding to the transition to the AF state. Similar findings are observed for magnetic fields up to 9 T applied perpendicular to the *c*-axis. According to studies conducted in ErB_4 [9], two field-induced transitions occur for fields applied parallel and perpendicular to the *c*-axis. At 1.5 K, the plateau state is maintained between 2 and 4 T along the *c*-axis and between 11.5 and 13.0 T along the *a*-axis. Therefore, if these magnetic transitions exist along the direction perpendicular to the *c*-axis, they were not observed in our lightly Er-doped materials, as our experimental measurements were conducted up to a maximum applied magnetic field of 9 T. When comparing the $M \times H$ curves along the *c*-axis for $Gd_{0.6}Er_{0.4}B_4$ with pure ErB_4, the transition to the plateau state in the $x = 0.4$ sample occurs at relatively higher magnetic fields, and this state is maintained within a narrow range of 4.5 to 5.3 T.

It is interesting to note that GdB_4 and TbB_4 are the only members of the RB_4 family that have the easy axis along the *ab*-plane. In the case of GdB_4, Gd's 4f shell is half filled, with $L = 0$, so the ions are in the s-state, and the anisotropy in the ordered phase comes mainly from the exchange interaction [31], which is small. It is suggested that this small magnetic anisotropy is the reason why no plateaus are observed in the $M \times H$ curves [32]. Therefore, doping with Er seems to be a convenient way to induce anisotropy in the magnetic properties of GdB_4. Our findings suggest that 40% of the substitution of Er for Gd is already enough to provoke the appearance of a plateau phase in the $M \times H$ curves.

4. Conclusions

In conclusion, we carried out a study of the thermal and magnetic properties of flux-grown $Gd_{1-x}Er_xB_4$ single crystals. This study revealed detailed magnetic transitions in both $x = 0.2$ and 0.4 compositions, including the full alignment of Er^{3+} magnetic moments for the magnetic field applied along the *c*-axis, and a metamagnetic transition corresponding to a plateau phase observed in the $x = 0.4$ sample.

While GdB4 and ErB4 compounds exhibit antiferromagnetic behavior with reversible magnetization isotherms and no magnetic hysteresis, the partial substitution of Er for Gd in the GdB4 lattice induced an anomalous ferromagnetic phase below the ordering temperature TN of the materials. This ferromagnetic phase exhibited significant anisotropy, with a pronounced manifestation along the *c*-axis. It is worth noting that the *c*-axis and the [110] direction correspond to the easy magnetization axes of ErB4 and GdB4 compounds, respectively.

Despite the lower Er content in the $Gd_{1-x}Er_xB_4$ ($x = 0.2$ and 0.4) samples, we observed moderately high values for the coercive field and remnant magnetization along the *c*-axis, which coincides with the easy axis for ErB_4. These intriguing features are likely due to the competing anisotropies. To further elucidate the origins of these interesting behavior, a comprehensive investigation of the physical properties of these single crystals is currently underway.

Author Contributions: Conceptualization, R.F.J.; formal analysis, S.H.M., and V.B.B.; investigation, S.H.M., F.A., R.F.J. and M.S.T.; resources, R.F.J.; writing—original draft preparation, S.H.M. and V.B.B.; writing—review and editing, F.A., R.F.J. and M.S.T.; supervision, R.F.J.; funding acquisition, R.F.J. All authors have read and agreed to the published version of the manuscript.

Funding: This research was funded by FAPESP (Grants No. 2013/07296–2, 2019/26141–6, 2022/02691–0, and 2022/10874–7), CNPq (Grant No. 301463/2019–0), and CAPES (Finance Code 001).

Data Availability Statement: The data presented in this study are openly available in Zenodo at https://doi.org/10.5281/zenodo.8152048 (accessed on 16 July 2023).

Acknowledgments: The authors thank the Laboratory of Crystallography, Instituto de Física, Universidade de São Paulo, Brazil, for the X-ray Laue diffraction work.

Conflicts of Interest: The authors declare no conflict of interest.

References

1. Post, B.; Moskowitz, D.; Glaser, F.W. Borides of Rare Earth Metals. *J. Am. Chem. Soc.* **1956**, *78*, 1800–1802. [CrossRef]
2. Buschow, K.H.J.; Creyghton, J.H.N. Magnetic Properties of Rare Earth Tetraborides. *J. Chem. Phys.* **1972**, *57*, 3910–3914. [CrossRef]
3. Bae, J.H.; Cho, K.K.; Lee, J.W.; Han, S.H.; Cho, B.K. Magnetic Entropy Changes for the Rotating Magnetocaloric Effect in RB_4 (R = Gd, Tb, Dy, Ho, Er, and Tm). *J. Magn. Magn. Mater.* **2023**, *576*, 170767. [CrossRef]
4. Kim, J.Y.; Cho, B.K.; Han, S.H. Anisotropic Magnetic Phase Diagrams of HoB_4 Single Crystal. *J. Appl. Phys.* **2009**, *105*, 07E116. [CrossRef]
5. Ye, L.; Suzuki, T.; Checkelsky, J.G. Electronic Transport on the Shastry-Sutherland Lattice in Ising-Type Rare-Earth Tetraborides. *Phys. Rev. B* **2017**, *95*, 174405. [CrossRef]
6. Yoshii, S.; Yamamoto, T.; Hagiwara, M.; Shigekawa, A.; Michimura, S.; Iga, F.; Takabatake, T.; Kindo, K. High-Field Magnetization of TmB_4. *J. Phys. Conf. Ser.* **2006**, *51*, 59–62. [CrossRef]
7. Iga, F.; Shigekawa, A.; Hasegawa, Y.; Michimura, S.; Takabatake, T.; Yoshii, S.; Yamamoto, T.; Hagiwara, M.; Kindo, K. Highly Anisotropic Magnetic Phase Diagram of a 2-Dimensional Orthogonal Dimer System TmB_4. *J. Magn. Magn. Mater.* **2007**, *310*, e443–e445. [CrossRef]
8. Sriram Shastry, B.; Sutherland, B. Exact Ground State of a Quantum Mechanical Antiferromagnet. *Phys. B+C* **1981**, *108*, 1069–1070. [CrossRef]
9. Michimura, S.; Shigekawa, A.; Iga, F.; Sera, M.; Takabatake, T.; Ohoyama, K.; Okabe, Y. Magnetic Frustrations in the Shastry–Sutherland System ErB_4. *Phys. B Condens. Matter* **2006**, *378–380*, 596–597. [CrossRef]
10. Will, G.; Schäfer, W.; Pfeiffer, F.; Elf, F.; Etourneau, J. Neutron Diffraction Studies of TbB_4 and ErB_4. *J. Less Common Met.* **1981**, *82*, 349–355. [CrossRef]
11. Siemensmeyer, K.; Wulf, E.; Mikeska, H.-J.; Flachbart, K.; Gabáni, S.; Mat'aš, S.; Priputen, P.; Efdokimova, A.; Shitsevalova, N. Fractional Magnetization Plateaus and Magnetic Order in the Shastry-Sutherland Magnet TmB_4. *Phys. Rev. Lett.* **2008**, *101*, 177201. [CrossRef]
12. Dublenych, Y.I. Ground States of the Ising Model on the Shastry-Sutherland Lattice and the Origin of the Fractional Magnetization Plateaus in Rare-Earth-Metal Tetraborides. *Phys. Rev. Lett.* **2012**, *109*, 167202. [CrossRef]
13. Blanco, J.A.; Brown, P.J.; Stunault, A.; Katsumata, K.; Iga, F.; Michimura, S. Magnetic Structure of GdB_4 from Spherical Neutron Polarimetry. *Phys. Rev. B* **2006**, *73*, 212411. [CrossRef]
14. Fisk, Z.; Maple, M.B.; Johnston, D.C.; Woolf, L.D. Multiple Phase Transitions in Rare Earth Tetraborides at Low Temperature. *Solid State Commun.* **1981**, *39*, 1189–1192. [CrossRef]
15. Regeciová, L.; Farkašovský, P. Magnetocaloric Effect in the Ising Model with RKKY Interaction on the Shastry–Sutherland Lattice. *Solid State Commun.* **2023**, *371*, 115251. [CrossRef]
16. Zhang, W.; Zhao, B.; Ni, N.; Xiang, H.; Dai, F.-Z.; Wu, S.; Zhou, Y. High Entropy Rare Earth Hexaborides/Tetraborides (HE REB_6/HE REB_4) Composite Powders with Enhanced Electromagnetic Wave Absorption Performance. *J. Mater. Sci. Technol.* **2021**, *87*, 155–166. [CrossRef]
17. Tao, P.; Ma, J.; Li, S.; Shao, X.; Wang, B. First-Principles Study of the Magnetic and Electronic Structure of NdB_4. *Materials* **2023**, *16*, 2627. [CrossRef]
18. Kang, B.Y.; Lee, S.S.; Song, M.S.; Cho, K.K.; Han, S.H.; Cho, B.K. Universality of Weak Ferromagnetism in the Magnetically Frustrated System $R_{1-x}Y_xB_4$. *Curr. Appl. Phys.* **2016**, *16*, 1001–1004. [CrossRef]
19. Gabani, S.; Flachbart, K.; Siemensmeyer, K.; Mori, T. Magnetism and Superconductivity of Rare Earth Borides. *J. Alloys Compd.* **2020**, *821*, 153201. [CrossRef]
20. Cullity, B.D.; Stock, S.R. *Elements of X-ray Diffraction*, 3rd ed.; Pearson: Fort Worth, TX, USA, 2014; ISBN 978-1-292-04054-7.
21. QLaue. Available online: https://sourceforge.net/projects/qlaue/ (accessed on 5 June 2023).
22. Masunaga, S.H.; Barbeta, V.B.; Jardim, R.F.; Becerra, C.C.; Torikachvili, M.S.; Rosa, P.F.S.; Fisk, Z. Anomalous Remnant Magnetization in Dilute Antiferromagnetic $Gd_{1-x}Y_xB_4$. *Phys. Rev. Mater.* **2018**, *2*, 084415. [CrossRef]
23. Toby, B.H. EXPGUI, a Graphical User Interface for GSAS. *J Appl Cryst* **2001**, *34*, 210–213. [CrossRef]
24. Shannon, R.D. Revised Effective Ionic Radii and Systematic Studies of Interatomic Distances in Halides and Chalcogenides. *Acta Cryst. A* **1976**, *32*, 751–767. [CrossRef]
25. Novikov, V.V.; Mitroshenkov, N.V.; Morozov, A.V.; Matovnikov, A.V.; Avdashchenko, D.V. Heat Capacity and Thermal Expansion of Gadolinium Tetraboride at Low Temperatures. *J. Appl. Phys.* **2012**, *111*, 063907. [CrossRef]

26. Novikov, V.V.; Morozov, A.V.; Matovnikov, A.V.; Mitroshenkov, N.V.; Avdashchenko, D.V.; Kuznetsov, S.V.; Kornev, B.I.; Marakhina, O.A.; Novikova, V.V.; Bordacheva, E.O. The Properties of Lattice, Electronic and Magnetic Subsystems of Erbium Tetraboride Based on Calorimetric Data at Temperatures of 2–300 K. *J. Alloys Compd.* **2013**, *581*, 431–434. [CrossRef]
27. Stout, J.W.; Catalano, E. Heat Capacity of Zinc Fluoride from 11 to 300 °K. Thermodynamic Functions of Zinc Fluoride. Entropy and Heat Capacity Associated with the Antiferromagnetic Ordering of Manganous Fluoride, Ferrous Fluoride, Cobaltous Fluoride, and Nickelous Fluoride. *J. Chem. Phys.* **2004**, *23*, 2013–2022. [CrossRef]
28. Gopal, E.S.R. *Specific Heats at Low Temperatures*, 1st ed.; Springer Science & Business Media: New York, NY, USA, 2012; ISBN 978-1-4684-9081-7.
29. Carlin, R.L. *Magnetochemistry*; Springer: Berlin/Heidelberg, Germany, 1986; ISBN 978-3-642-70735-3.
30. Song, M.S.; Cho, K.K.; Lee, J.W.; Cho, B.K. Abnormal Field-Dependence of Magnetocaloric Effect in ErB_4 and TmB_4. *AIP Adv.* **2020**, *10*, 025219. [CrossRef]
31. Lovesey, S.W.; Rodríguez, J.F.; Blanco, J.A.; Brown, P.J. Phase Transitions, Noncollinear Magnetism, and Magnetoelectric Symmetry in Gadolinium Tetraboride. *Phys. Rev. B* **2004**, *70*, 172414. [CrossRef]
32. Baranovskiy, A.; Grechnev, A. Electronic Structure and Exchange Interactions in GdB_4. *J. Magn. Magn. Mater.* **2015**, *375*, 96–99. [CrossRef]